PHYSICAL REVIEW B **67**, 165215 (2003)

Spin resonance investigations of Mn^{2+} in wurtzite GaN and AlN films

T. Graf,* M. Gjukic, M. Hermann, M. S. Brandt, and M. Stutzmann
Walter Schottky Institut, Technische Universität München, Am Coulombwall, 85748 Garching, Germany

O. Ambacher
Zentrum für Mikro- and Nanotechnologien, Technische Universität Ilmenau, Gustav-Kirchhoff-Strasse 1, 98684 Ilmenau, Germany

(Received 19 August 2002; revised manuscript received 16 December 2002; published 30 April 2003; publisher error corrected 8 May 2003)

High quality Mn-doped GaN and AlN films grown by molecular beam epitaxy have been investigated with *X*-band electron spin resonance (ESR). The observed resonance patterns are well described by the spin Hamiltonian for isolated $^{55}Mn^{2+}$ centers with electronic spin $S=5/2$ and nuclear spin $I=5/2$. Isotropic g factors $g=2.000$ and hyperfine parameters $A=-69\ \mathrm{G}\times g\mu_B$ are observed both in GaN and AlN, while the fine-structure parameters vary from $D_{\mathrm{GaN}}=-218\ \mathrm{G}\times g\mu_B$ for strongly strained GaN films to $D_{\mathrm{GaN}}=-236\ \mathrm{G}\times g\mu_B$ for almost relaxed GaN films, and to $D_{\mathrm{AlN}}=-648\ \mathrm{G}\times g\mu_B$ for relaxed AlN films. At intermediate orientations of the crystalline c axis with respect to the magnetic field, intermixing occurs between the nuclear spin eigenstates due to off-diagonal elements in the spin Hamiltonian, which strongly enhances the transition probabilities of usually forbidden ESR transitions with $|\Delta m_I|>0$. This is confirmed experimentally as well as by numerical simulations. It is concluded that Mn^{2+} impurities are present as isolated, paramagnetic centers at the investigated doping concentration of $10^{20}\ \mathrm{cm}^{-3}$, without any evidence for electrostatic or magnetic coupling to extended valence band states, which is a prerequisite of ferromagnetic exchange required for spintronic devices.

DOI: 10.1103/PhysRevB.67.165215 PACS number(s): 76.30.Fc, 71.55.Eq, 75.50.Pp

I. INTRODUCTION

The electronic and magnetic properties of transition metal impurities in wide band-gap semiconductors currently attract considerable scientific interest because of their potential use in spintronic devices at high doping concentrations.[1] Room temperature ferromagnetism was predicted for transition-metal-doped GaN, ZnO, and diamond, extrapolating from the Curie temperature $T_C=110$ K of the dilute magnetic semiconductor (DMS) material $Ga_{0.95}Mn_{0.05}As$.[2] In this material, itinerant holes are believed to mediate the ferromagnetic exchange between localized Mn spins.

Information about the microscopic configuration of transition metal centers has been extracted from their paramagnetic resonance in many crystals, ranging from the purely covalent group IV semiconductors to the ionic group I–VII salts. Mn-related centers have been investigated in several III–V compounds, but the information on the oxidation states of substitutional Mn in GaN and AlN is still incomplete. The aim of this paper is the determination of the spin properties of the Mn ground state in epitaxial GaN and AlN films. Up to a doping level of about $10^{20}\ \mathrm{cm}^{-3}$, we detect only isolated $S=5/2$ centers by electron spin resonance (ESR). In particular, we find no effective-mass-like Mn^{2+}-hole complexes in Mn-doped group III nitrides, contrary to what has been reported previously for bulk GaAs:Mn.[3] The observed axial distortion at the localized Mn^{2+} states in wurtzite GaN and AlN indicates that also for possibly itinerant states in these materials a polaronic model is more appropriate than the mean-field Zener model used to describe the ferromagnetism of GaAs.[4]

Up to now, ESR identification of Mn^{2+} in GaN has only been reported in unintentionally doped bulk crystals prepared by the sublimation sandwich method at small Mn concentrations of $10^{17}\ \mathrm{cm}^{-3}$.[5–7] This growth method is quite useful for the preparation of large GaN crystals;[8] however, most device-quality epitaxial GaN films are presently grown by molecular beam epitaxy (MBE) or metal-organic chemical vapor deposition (MOCVD) because of higher purity and better doping control. Although at first sight the ESR spectra of our highly doped MBE-grown GaN:Mn^{2+} films are similar to those reported for the lower-doped bulk crystals, the extracted fine- and hyperfine-structure parameters differ significantly. The differences in the axial fine-structure parameter can be dominantly ascribed to the biaxial strain from the sapphire substrate. Because the degree of relaxation varies with the film thickness and the growth conditions in our samples, the influence of the crystal field on the Mn^{2+} ground state can be studied without the application of external pressure. Some features of the numerical simulation reported in Refs. 5–7 are neither present in the experimental spectra nor in our numerical results. However, some additional "forbidden" transitions neglected in Refs. 5–7 are prominent in our experimental spectra. To review their origin and to describe the spin properties of Mn^{2+} in GaN and AlN more accurately, a refined experimental and numerical investigation of the spin Hamiltonian is presented here.

So far, only few other ESR studies on Mn in group-III nitrides are available. In addition to Refs. 5–7, Mn-related ESR was reported in microcrystalline GaN grown by the ammonothermal method and doped intentionally with different concentrations of Mn.[9] In this study, the identification was restricted to the isotropic part of the ESR spectrum, and therefore no direct evidence for the Mn oxidation state could be extracted. Intentionally doped GaN:Mn crystals have been prepared by MOCVD (Refs. 10 and 11) and MBE,[12,13] but to our knowledge, these samples have not been studied by ESR yet. In polycrystalline AlN, some Mn-related ESR spectra with *g* factors in the range of 1.8–10 were reported together with Mn^{2+}- and Mn^{4+}-related photoluminescense.[14] Again, no ESR anisotropy of Mn-related centers in AlN crystals was reported up to now, which is necessary for a detailed analysis of the spin Hamiltonian.

II. EXPERIMENTAL DETAILS

The GaN:Mn and AlN:Mn films investigated here were grown epitaxially on $\mathrm{Al_2O_3}$ substrates by plasma induced molecular beam epitaxy (PIMBE) with a layer thickness of 1–1.5 μm. The growth temperatures were 690–820 °C for GaN:Mn and for codoped GaN:Mn:Si films, and about 850 °C for AlN:Mn films, which is somewhat lower than the temperatures used for the growth of optimized GaN and AlN layers.[15] The doping concentrations $[\mathrm{Mn}]_{\mathrm{GaN}}\approx 10^{20}\ \mathrm{cm}^{-3}$ and $[\mathrm{Mn}]_{\mathrm{AlN}}\approx 10^{19}\ \mathrm{cm}^{-3}$ were determined by Elastic Recoil Detection (ERD).[16] Lowering the GaN growth temperatures did not lead to a significant increase of the Mn incorporation, but gave rise to the precipitation of $\mathrm{Mn_3N_2}$ clusters,[17] which were clearly observed in samples grown at 690 °C. The crystalline quality and the lattice constants of the epitaxial films were investigated by x-ray diffraction. Typically, the full width at half maximum (FWHM) of the (002) reflex for GaN:Mn (AlN:Mn) layers was about 500 (800) arcsec for rocking curves (Ω scans) and 50 (100) arcsec for 2Θ–Ω scans, independent of the doping concentration. These widths confirm the structural quality of the GaN and AlN films. They would correspond to variations of the out-of-plane lattice constant *c* of about 0.04%, if they were caused by a spread of *c* only.

As reported, e.g., in Ref. 18, the lattice mismatch to the sapphire substrate and the mismatch of the respective thermal expansion coefficients causes biaxial strain in GaN and AlN thin films. Additionally, hydrostatic strain is expected at high doping concentrations. Therefore, the in-plane lattice constant *a* of expitaxial GaN films is compressed with respect to the bulk value $a_0=3.1878$ Å, and *c* expanded with respect to $c_0=5.1850$ Å.[18] These changes were monitored in reciprocal space maps of the asymmetric (2025) reflex for all samples investigated here. The relative deviations of the in-plane lattice constant $\varepsilon_a=(a-a_0)/a_0$ varied from -0.04% to -0.25%, and the deviations in growth direction $\varepsilon_c=(c-c_0)/c_0$ from 0.03% to 0.15%, with the codoped GaN:Mn:Si samples grown at 820 °C showing the largest strain. A linear dependence between both relative changes with $\varepsilon_c/\varepsilon_a=-0.6\pm 0.02$ is observed for the investigated films, which corresponds to the effective Poisson ratio $\nu=-(\varepsilon_c/\varepsilon_a)/[(\varepsilon_c/\varepsilon_a)-2]=0.23$ reported earlier in Ref. 18. In the following, we first analyze in detail the spin Hamiltonian parameters of the pure $\mathrm{GaN{:}Mn^{2+}}$ and $\mathrm{AlN{:}Mn^{2+}}$ films, which are mostly relaxed. Then, these values are compared with the spin Hamiltonian parameters of the more strained $\mathrm{GaN{:}Mn^{2+}{:}Si}$ films and those of the bulk $\mathrm{GaN{:}Mn^{2+}}$ crystal of Refs. 5–7.

The ESR spectra were recorded with a Bruker ESP-300 system, using a standard *X*-band TM_{102} resonator. The sample temperature was controlled in the range from 2.8 to 300 K with a helium flow cryostat. The orientation of the sample with respect to the magnetic field could be checked conveniently with the help of the known anisotropic ESR signals from the sapphire substrate. Most of these background resonances are saturated easily at sufficiently high microwave power and low temperatures and, thus, are suppressed in the experimental spectra.

III. RESULTS

A. Spin Hamiltonian of the Mn^{2+} ground state

Starting from the $[\mathrm{Ar}]3d^5 4s^2$ electronic configuration of free Mn atoms, Mn^{2+} usually denotes the Mn oxidation state with a half-filled $3d^5$ shell. Within a semiconductor lattice, this formally twofold ionic charge is distributed over the neighboring host valences and screened by the valence band electrons, so that the ionization threshold is effectively reduced in comparison to free Mn ions.[19,20] The electronic spin $S=5/2$ of the five $3d$ electrons of the Mn^{2+} Kramers ion is conserved and typically combined to a ${}^6\mathrm{A}_1$ ground-state configuration without orbital momentum. This ground state is additionally coupled to the nuclear spin $I=5/2$ of the natural isotope ${}^{55}\mathrm{Mn}$.

Generally, it is incorrect to employ crystal field theory to describe the zero-field splitting of impurity ground states in semiconductors because of the presence of continuum electronic states that hybridize with the atomic Mn orbitals.[20,21] However, the phenomenological form of the crystal field spin Hamiltonian is still correct, even if the true origin of the occurring parameters fails to agree with real crystal fields.[21] Therefore, the effective Mn^{2+} ground state manifold of $(2S+1)(2I+1)=36$ spin states can be described by the Hamiltonian[22–25]

$$\begin{aligned}\mathcal{H}=&\ \mu_B\vec{H}g\vec{S}+D\left(S_z^2-\frac{35}{12}\right)+\vec{S}A\vec{I}\\&+\frac{1}{6}a\left(S_\xi^4+S_\eta^4+S_\zeta^4-\frac{707}{16}\right)\\&+\frac{7}{36}F\left(S_z^4-\frac{95}{14}S_z^2+\frac{81}{16}\right)+P\left(I_z^2-\frac{35}{12}\right)-\mu_B\vec{H}g_I\vec{I}\end{aligned}\tag{1}$$

with Bohr's magneton μ_B, and all other parameters introduced in the following. A so-called Breit-Rabi diagram of the eigenenergies plotted as a function of the external field $\vec{H}\|\vec{e}_z\|c$ (lattice vector of the wurtzite crystal) is shown in Fig. 1 using the parameters for $g,D,A,\ldots$ determined for $\mathrm{AlN{:}Mn^{2+}}$ later in this paper. The 36 eigenstates are denoted by m_S and m_I according to their S_z and I_z quantum numbers at large magnetic fields. As indicated, the allowed transitions follow the selection rule $\Delta m_S=\pm 1$ and $\Delta m_I=0$ in this orientation. In *X*-band ESR experiments, the total eigenenergies are mainly determined by the Zeeman energy on the order of 100 μeV at $H=3300$ G. The axial crystal field is parametrized by *D*, which is dominating the fine structure of the levels in the zero-field limit. It is distributing the electronic spin states into three Kramers doublets separated by about 20 μeV, as indicated in Fig. 1. The hyperfine interaction *A*

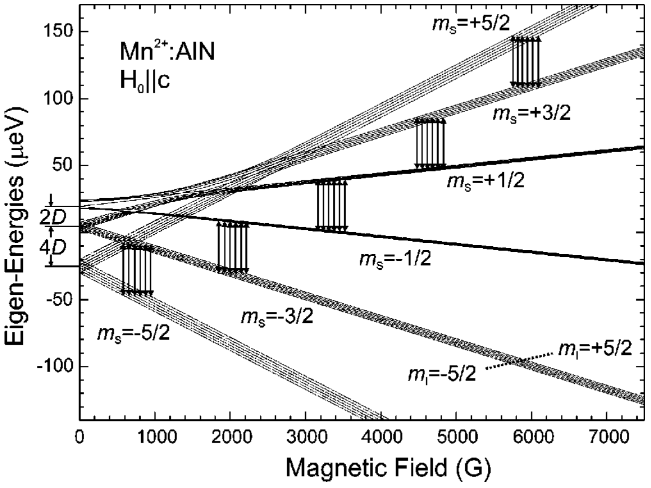

FIG. 1. Breit-Rabi Diagram for Mn^{2+} in AlN with the magnetic field oriented parallel to the *c* axis of the film. At this orientation, the spin quantization axis is well oriented along the *z* direction at low and high magnetic fields because of the combined effect of the Zeeman and the axial fine-structure interactions. The parameters used are $g_{\mathrm{AlN}}\approx 2.000$, $D_{\mathrm{AlN}}\approx -8$ μeV, $A_{\mathrm{AlN}}\approx -0.8$ μeV, and $h\nu\approx 40$ μeV.

of the electronic spin with the nuclear spin of ^{55}Mn further splits the spin levels by energies on the order of 2 μeV. The fine-structure parameters *a* and *F* of the cubic crystal field for $S=5/2$ states are even smaller and on the order of 0.1 μeV only. S_ξ, S_η, and S_ζ are the projections of $\vec{S}$ onto the axis of the cubic crystal field discussed below. Further contributions such as the nuclear Zeeman interaction characterized by $g_I \approx 0.0004g$ and the nuclear quadrupolar interaction characterized by *P* give rise to even smaller energy corrections. The nuclear spin parameters g_I and *P* cancel out for the "allowed" electron-spin-resonance transitions, for which m_I remains unchanged, but they contribute significantly to the positions of the "forbidden" transition doublets of Eq. (10). Therefore, they should be included in Eq. (1). However, since the nuclear properties g_I and *P* are extremely similar in different materials, the values for both parameters were taken from ZnO (Ref. 26) to also describe the Mn^{2+} states in GaN and AlN.

In the ideal wurtzite structure, the coordination of the four nearest nitrogen neighbors is tetrahedral, but the symmetry is lowered to C_{3v} in the group-III nitrides. Consequently, the axial distortion, which is expressed by the crystal field parameter *D*, is assumed to be oriented along the sample *c* axis in agreement with the observed ESR signals discussed below. For the notation (1) of the spin Hamiltonian, the *z* coordinate axis is chosen along this axis of *D* and fixed with respect to the sample, although the axis of spin quantization will rather be oriented along $\vec{H}$. To investigate all possible relative orientations, the angle θ between $\vec{H}$ and the *c* axis of the sample is varied between 0 and 90° by a rotation of $\vec{H}$ within the $[1\bar{2}10]$ and $[10\bar{1}0]$ planes, as shown in Fig. 2. For the tetrahedral substitutional sites, those two rotations are indistinguishable in quadratic terms like the Zeeman and Hyperfine interaction, as the corresponding energy ellipsoids do not reflect the threefold crystalline symmetry around *c*. This is different for the cubic crystal field described with three perpendicular axes ξ, η, and ζ, which are tilted by 35.26° with respect to the [0001] plane and oriented parallel to the edges of the cubes, as indicated in Fig. 2.[24–26] There are two distinct cubes for the *A* and *B* site of the wurtzite *AB* stacking sequence, each containing one central atom and four nearest tetrahedral neighbors on the corners. The orientation of these cubes with respect to the external field $\vec{H}$ can be expressed by a single parameter $\phi=l^2m^2+m^2n^2+n^2l^2$ with l,n,m being the direction cosines of ξ, η, and ζ, respectively, with respect to the field axis.[22,25] As can be deduced from Fig. 2, the parameter ϕ is symmetric with respect to the sign of θ for rotations within the $[10\bar{1}0]$ plane and asymmetric for rotations within the $[1\bar{2}10]$ plane for *A* and *B* sites, respectively. Geometrical considerations result in

$$\phi_{10\bar{1}0}=\frac{1}{96}[21+4\cos(2\theta)+7\cos(4\theta)],$$

$$\phi_{1\bar{2}10}=\phi_{10\bar{1}0}\pm\frac{\sqrt{2}}{96}[8\sin(2\theta)-4\sin(4\theta)]. \qquad (2)$$

As the anisotropy of the cubic crystal field is described in terms of ϕ only, its symmetry reappears in the solutions of the spin Hamiltonian. The maximum difference between the eigenenergies of the magnetically inequivalent *A* and *B* sites of the wurtzite lattice is expected for a maximal splitting of $\phi_{[1\bar{2}10]}$ at $\theta=60°$ in the $[1\bar{2}10]$ plane.[25]

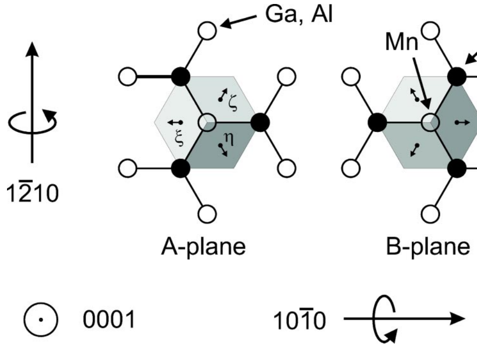

FIG. 2. The two magnetically nonequivalent *A* and *B* lattice sites of the wurtzite lattice. The largest cubic fine-structure splitting between the Mn^{2+} ESR of the two sites is expected for magnetic fields tilted by $\theta=60°$ from the [0001] axis towards $[10\bar{1}0]$. However, this splitting is below the experimental linewidth of the experimental data reported here.

B. Analysis of the ESR spectra for $\vec{H}\|c$

Most of the properties of Mn^{2+} in GaN and AlN are conveniently extracted from the spectra of Fig. 3 at $\theta=0°$, where the splitting of adjacent lines is maximum. In this orientation, the electronic part of the spin Hamiltonian can be diagonalized analytically, as the axis of the crystal field *D* coincides with the magnetic field axis.[24,25] The parameters from the analysis of the spectrum at $\theta=0°$ are then used in

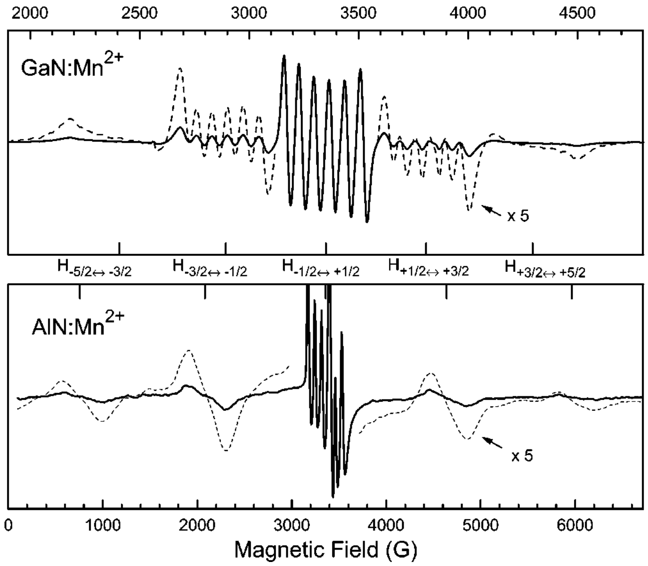

FIG. 3. X-band ESR spectra of Mn^{2+} with the magnetic field oriented parallel to the c axis of GaN and AlN at $T=6$ K. In both spectra, five $(2S)$ groups of six $(2I+1)$ hyperfine satellites indicate the presence of ^{55}Mn^{2+}. Increased broadening of the outer fine-structure groups reveals fluctuations in the zero-field splitting of about 5%. In the spectra shown, microwave saturation helps suppress the background ESR dominated by impurities in the sapphire substrate.

Sec. III C to verify the full anisotropy of the spin Hamiltonian. Neglecting hyperfine interactions, one obtains the analytical eigenenergies

$$\begin{aligned}W_{\pm 5/2}&=\pm g\mu_B H+D/3-(a-F)/2\\&\quad\pm\sqrt{[\pm(3/2)g\mu_B H+3D+(a-F)/6]^2+(20/9)a^2},\\W_{\pm 3/2}&=\pm(3/2)g\mu_B H-(2/3)D+(a-F),\\W_{\pm 1/2}&=\mp g\mu_B H+D/3-(a-F)/2\\&\quad\pm\sqrt{[\pm(3/2)g\mu_B H-3D-(a-F)/6]^2+(20/9)a^2}.\end{aligned}\tag{3}$$

According to the first-order approximation of large microwave energies $h\nu\gg|D|\gg|a-F|$, the cubic crystal field parameters always occur in a combination $a-F$, so that additional measurements at intermediate angles are required for the determination of these parameters separately. The solutions for the resonance condition $h\nu=W_{m_S}-W_{m_S-1}$ define the magnetic-field positions $H_{m_S\leftrightarrow m_S-1}$ of the resonances $|m_S\rangle\leftrightarrow|m_S-1\rangle$. The parameters $g=h\nu/(\mu_B H_{+1/2\leftrightarrow -1/2})\approx 2.000$, and D and $a-F$ are then calculated in terms of these fields, which are indicated in Fig. 3 by the centers of gravity of the fine-structure resonance groups:

$$\begin{aligned}|D|&=(g\mu_B/56)|5(H_{+5/2\leftrightarrow +3/2}-H_{-3/2\leftrightarrow -5/2})\\&\quad+4(H_{+3/2\leftrightarrow +1/2}-H_{-1/2\leftrightarrow -3/2})|,\\|a-F|&=(g\mu_B/28)|-3(H_{+5/2\leftrightarrow +3/2}-H_{-3/2\leftrightarrow -5/2})\\&\quad+6(H_{+3/2\leftrightarrow +1/2}-H_{-1/2\leftrightarrow -3/2})|.\end{aligned}\tag{4}$$

For the spectrum of a GaN:Mn^{2+} film with $c=5.187$ Å and $a=3.187$ Å shown in Fig. 3, we find

$$|D_{\text{GaN}}|=g\mu_B(236\pm 2)\text{G}=hc\times 220\times 10^{-4}\ \text{cm}^{-1},$$

$$|a-F|_{\text{GaN}}=g\mu_B(6\pm 3)\text{G}=hc\times 5\times 10^{-4}\ \text{cm}^{-1},$$

and correspondingly for an AlN:Mn^{2+} film with $c=4.981$ Å and $a=3.112$ Å

$$|D_{\text{AlN}}|=g\mu_B(648\pm 3)\text{G}=hc\times 605\times 10^{-4}\ \text{cm}^{-1},$$

$$|a-F|_{\text{AlN}}=g\mu_B(10\pm 4)\text{G}=hc\times 9\times 10^{-4}\ \text{cm}^{-1}.$$

In units of frequency, the larger fine-structure zero-field splitting $\delta\approx 4|D|$ between the electronic Kramers doublets with $|m_S|=3/2$ and $|m_S|=5/2$ at $H=0$ is obtained as $\delta\approx 0.66$ GHz for GaN and $\delta\approx 1.8$ GHz for AlN. As experimentally the outer fine-structure splittings $|H_{+5/2\leftrightarrow +3/2}-H_{+3/2\leftrightarrow +1/2}|$ and $|H_{-1/2\leftrightarrow -3/2}-H_{-3/2\leftrightarrow -5/2}|$ are larger than the inner splittings $|H_{+3/2\leftrightarrow +1/2}-H_{+1/2\leftrightarrow -1/2}|$ and $|H_{+1/2\leftrightarrow -1/2}-H_{-1/2\leftrightarrow -3/2}|$, it can be deduced from Eq. (3) that D and $a-F$ have opposite signs. The relative sign of D with respect to g, the latter of which is assumed to be positive, has to be deduced by other means, as discussed below.

Up to now, the hyperfine interaction between electronic and nuclear spins has been neglected in the calculation of the eigenenergies. Treating this additional interaction as a small perturbation, the magnetic-field offsets $\Delta h_{m_S,m_I\leftrightarrow m_S-1,m_I}$ of the transitions $|m_S,m_I\rangle\leftrightarrow|m_S-1,m_I\rangle$ from the transitions $|m_S\rangle\leftrightarrow|m_S-1\rangle$ resulting from Eq. (3) have been calculated to third order in A in Ref. 26:

$$\begin{aligned}&\Delta h_{m_S,m_I\leftrightarrow m_S-1,m_I}\\&\quad=H_{m_S,m_I\leftrightarrow m_S-1,m_I}-H_{m_S\leftrightarrow m_S-1}\\&\quad=-\frac{A}{g\mu_B}\Bigg\{m_I+\frac{A}{h\nu}[(m_S-1/2)m_I+1/2(35/4-m_I^2)]\\&\qquad+\frac{A^2}{(h\nu)^2}[(35/4-m_I^2)(2m_S-1)\\&\qquad-(1/2)m_I(35/4-3m_S^2+3m_S-2)]\\&\qquad+\frac{AD}{(h\nu)^2}[(35/4-m_I^2)(2m_S-1)\\&\qquad-m_I(35/4-m_S^2+m_S-1)]\Bigg\}.\end{aligned}\tag{5}$$

The hyperfine constant $|A|$ is given approximately by the splitting of about 70 G within one of the fine-structure groups. At X-band energies, higher-order terms are shifting the hyperfine resonances significantly, increasing both the apparent g factor and the effective hyperfine splitting. In Fig.

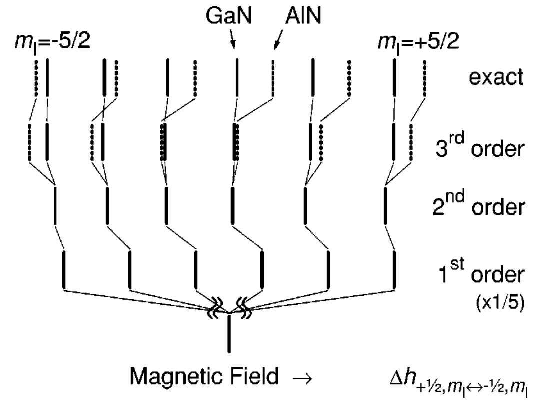

FIG. 4. For the Mn^{2+} spin system with both fine and hyperfine interactions, the resonance positions $H_{1/2\leftrightarrow-1/2}$ without nuclear spin are shifted by $h_{1/2,m_I\leftrightarrow-1/2,m_I}$, defined in Eq. (5) according to perturbation theory. The numerical calculation shows that mixing terms with the axial crystal field D of higher order become important in AlN:Mn^{2+} even at $\theta=0°$. The first-order splitting has been reduced to $A/5$ in this plot.

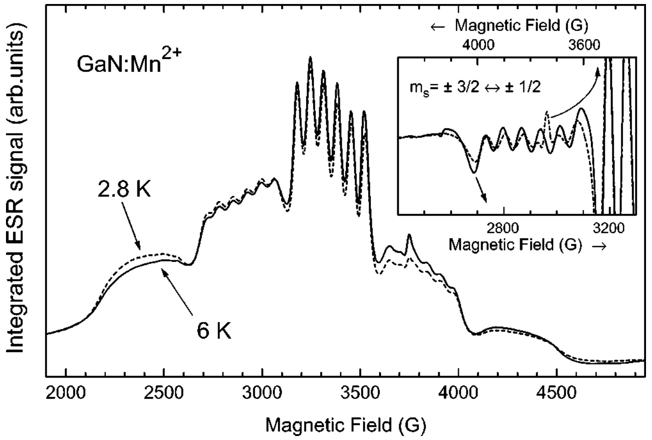

FIG. 5. Integrated GaN:Mn^{2+} spectra with the intensities corrected for the measurement temperature. The intensity ratio of the fine-structure groups is consistent with the ideal ratio 5:8:9:8:5 of an $S=5/2$ spin system. The intensity ratio at lower temperatures requires the assignment of these transitions to the m_S quantum numbers, as shown in Fig. 1. Microwave power has been reduced in these spectra in order to avoid microwave saturation. Therefore, some substrate resonances, e.g., a narrow line at 3750 G are not suppressed completely. The inset shows that second-order effects increase the hyperfine splitting of the low-field transitions $|m_S=-1/2\rangle\leftrightarrow|m_S=-3/2\rangle$ compared to the transitions $|m_S=3/2\rangle\leftrightarrow|m_S=1/2\rangle$, which have been plotted on a reversed magnetic-field axis. Therefore, the sign of A is determined to be negative, as that of D.

4, the resonance positions of the $m_S=1/2$ central fine-structure group are shown according to first-, second-, and third-order perturbation theory, and to the result of a numerical diagonalization of the complete spin Hamiltonian (1) for GaN and AlN, respectively. The numerical deviations of $\Delta h_{m_S,m_I\leftrightarrow m_S-1,m_I}-A/(g\mu_B)$ within this group are on the order of -6 to 0 G (-7 to $+7$ G) for GaN:Mn^{2+} (AlN:Mn^{2+}). The constant first-order splitting $A/(g\mu_B)$ has been reduced by a factor of 5 in Fig. 4 for better visibility of the higher-order effects. Obviously, the change in $|D|$ between both materials influences both the average positions, as well as the splitting of the central hyperfine sextet. According to the exact numerical calculations, $|A|=g\mu_B(69\pm1)$ G$=hc\times65\times10^{-4}$ cm^{-1} is obtained both for the GaN and AlN spectra of Fig. 3. After calibration of the magnetic-field positions with diphenyl-picrylhydrazyl (DPPH, $g=2.0036$), corrected g-factors $g=1.9994\pm0.0008$ for Mn^{2+} in GaN and $g=2.0004\pm0.0008$ in AlN are obtained.

For other transitions than $|+1/2,m_i\rangle\leftrightarrow|-1/2,m_i\rangle$, also the second-order corrections of Eq. (5) modify the effective hyperfine splitting, as they contain terms proportional to m_I. From the differences in hyperfine splitting, the relative sign of A with respect to that of D can be determined, as, e.g., the transitions $H_{+3/2\leftrightarrow+1/2}$ are shifted towards lower or higher magnetic field compared to $H_{+1/2\leftrightarrow-1/2}$ for positive or negative sign of D, respectively. To illustrate this, the spectrum of GaN:Mn^{2+} has been reversed in the inset of Fig. 5 in a way that some inner and outer hyperfine pairs overlap. For these groups, a larger splitting between adjacent hyperfine lines is observed at lower magnetic fields (full line) than in the reversed signal that occurs at higher magnetic fields (dashed line). The consequently stronger overlap of the high-field satellites is also responsible for their smaller ESR amplitude compared to the low-field satellites. These observations show that the sign of A is negative, if the transition $|+3/2,m_I\rangle\leftrightarrow|+1/2,m_I\rangle$ occurred at higher magnetic fields, i.e., if D was negative. Such a combination of negative D and A is depicted in the level diagram of Figs. 1 and 4.

However, it still remains to be shown that D is indeed negative in GaN and AlN. To determine the sign of D, one needs to clarify whether the transitions with positive m_S occur at high or low magnetic fields. Because the transition intensity $I_{m_S\leftrightarrow m_S-1}$ is proportional to the population difference between the levels $|m_S\rangle$ and $|m_S-1\rangle$, the situations for positive and negative D can be distinguished at low temperatures. Below microwave saturation, and for $k_BT\gg h\nu\gg|D|$, the thermal occupation of the levels $|m_S\rangle$ and $|m_S-1\rangle$ is given by the Boltzmann series[23]

$$I_{m_S\leftrightarrow m_S-1}\propto\frac{N_{m_S-1}-N_{m_S}}{\sum_n N_n}=\frac{1-\exp\left(\frac{-h\nu}{k_BT}\right)}{\sum_n \exp\left(\frac{W_{m_S-1}-W_n}{k_BT}\right)}\approx\frac{1}{6}\left(\frac{h\nu}{k_BT}\right)-\frac{m_S-1/2}{6}\left(\frac{h\nu}{k_BT}\right)^2. \qquad (6)$$

To first order in $h\nu/k_BT$, the occupation differences follow Curie's law for all levels, but as energetically lower pairs of levels have both a higher population as well as a higher difference in population, their population difference and ESR absorption are larger in second order. At X-band frequencies, $h\nu/k_B\approx0.43$ K, so that at 2.8 K, which is the lowest temperature achievable with our cryostat, we expect relative second-order changes of about 30% for the outer transitions $|\pm5/2,m_I\rangle\leftrightarrow|\pm3/2,m_I\rangle$ and about 15% for the inner transi-

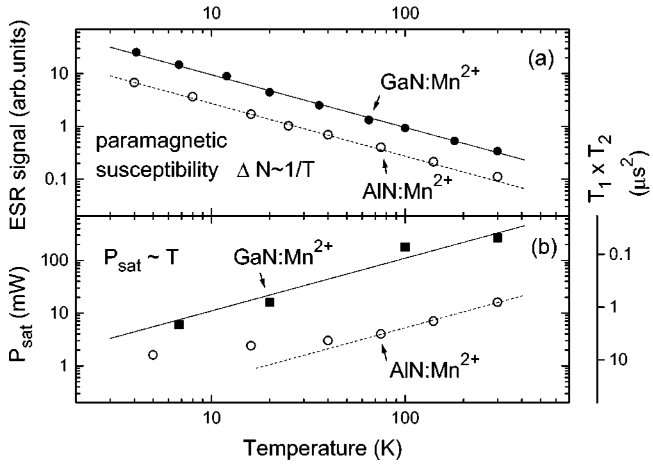

FIG. 6. Temperature dependence of (a) the ESR signal intensity and (b) the microwave saturation power, which is representative for the spin relaxation rates. The GaN:Mn^{2+} and AlN:Mn^{2+} ESR signals can be traced up to room temperature, indicating a low coupling of the Mn^{2+} spins to the surrounding lattice.

tions $|\pm 3/2,m_I\rangle \leftrightarrow |\pm 1/2,m_I\rangle$. Two integrated ESR spectra recorded at 2.8 and 6 K are shown normalized for the first-order Curie term in Fig. 5. The satellites in the region of lower magnetic fields grow faster than linearly in $h\nu/k_BT$ with decreasing temperature. Thus, they can be identified to belong to negative m_S. According to Fig. 1, this ordering of the fine-structure lines indicates a negative sign of D. From the earlier conclusions about the relative signs, A follows to be negative and $a-F$ to be positive, respectively.

As shown in Fig. 6, the spin resonance signal of Mn^{2+} in GaN and AlN can be measured up to room temperature. Within the experimental errors, no change was observed in the spin parameters and densities. Within the accessible temperature range, the paramagnetic susceptibility is well described by Curie's law, confirming the presence of an unchanged amount of isolated Mn^{2+} states below their ionization temperature [Fig. 6(a)]. The inhomogeneous linewidth of the central fine-structure group, which is about 30 G in GaN and about 15 G in AlN, did not change up to room temperature, which indicates a small contribution of spin-lattice relaxation processes in group-III nitrides to the linewidth. By the continuous saturation method, it is possible to obtain a rough estimate of the product $T_1 \times T_2$ of the spin-lattice relaxation time T_1 and the spin-spin relaxation time T_2, as displayed in Fig. 6(b). The observed approximately inverse proportionality to temperature would be consistent with a direct spin-lattice relaxation process without a phonon bottleneck.

The resonances of the central fine-structure group are well resolved in the sample orientation $\vec{H}\|c$, while the hyperfine resonances of the fine-structure satellite groups tend to overlap each other. As any spread due to a mosaic structure of the GaN film is small for orientations of H parallel to the principal crystalline axis, the excess linewidth of these satellites is most probably caused by an inhomogeneous distribution of fine-structure constants. The good agreement of the experimental ESR intensities and magnetic-field positions at $\vec{H}\|c$ with simulated spectra for a Lorentzian distribution of axial crystal fields D with a FWHM of 15 $G\times g\mu_B$ is shown in Fig. 7. According to Eq. (3), the separation of the fine-structure satellites from the unperturbed resonance position $H_{-1/2\leftrightarrow+1/2}$ is roughly proportional to D, so that the broadening of the fine-structure satellites is proportional to the variation of that separation for a distribution of D. As the central transition group is best resolved at intermediate orientations, where the magnetic-field separation of the fine-structure groups is small, possibly also fluctuations of the cubic crystal field parameters a and F must be considered. These variations of the crystal field are probably caused by residual inhomogeneous strains within the GaN layers.[5–7,22] It would be interesting to compare this with independent measurements of local strain, e.g., from micro-Raman spectroscopy or excitonic photoluminescence. No additional broadening due to electrostatic or magnetic interaction with neighboring Mn centers, as claimed in Ref. 9, was observed at the Mn concentrations of our GaN films. Despite the differences in amplitude, the same resonance positions are obtained for spectra simulated for an average crystal field parameter and for the distribution shown in Fig. 7. Therefore, neglecting linewidth effects, the following simulations for arbitrary sample orientation consider the average crystal field parameters only.

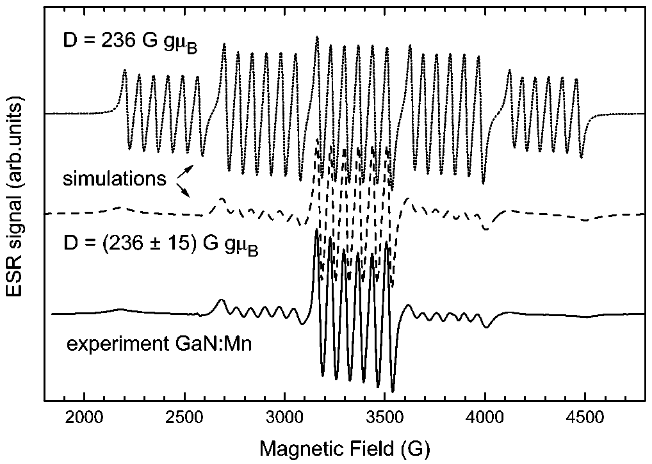

FIG. 7. Simulated and measured ESR spectra of GaN:Mn^{2+} for the sample orientation $\vec{H}\|c$. The upper spectrum (dotted line) was simulated for a single axial crystal field $D=236\ G\times g\mu_B$ and a residual linewidth of 25 G. A weighted average of similar spectra for a Lorentzian distribution of axial crystal parameters around 236 $G\times g\mu_B$ with a full width at half maximum of 30 $G\times g\mu_B$ results in the middle spectrum (dashed line), which is very similar to the experimental spectrum shown at the bottom (solid line).

Due to the differences in linewidth, the relative intensities of the fine-structure groups can be compared best after numerical double integration. The theoretical intensity for the five transition groups $|m_S \leftrightarrow m_S-1\rangle$ is proportional to the transition matrix elements from time-dependent perturbation theory. In the strong field limit, they are given by $S(S+1)-m_S(m_S-1)$.[22,23] Therefore, with $S=5/2$, the intensity ratios for the five fine-structure transition groups are 5:8:9:8:5,

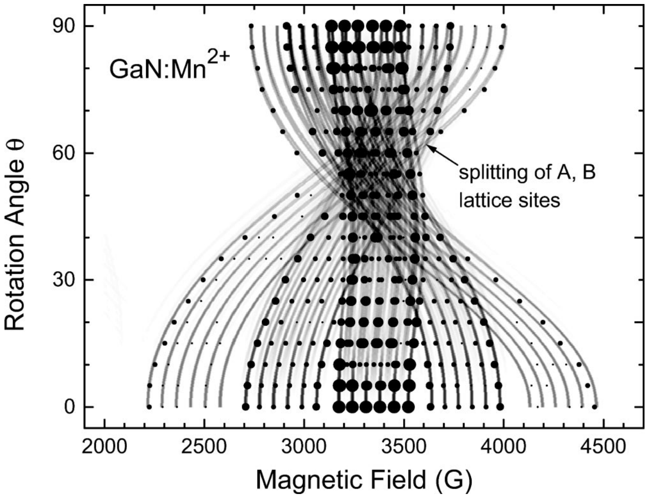

FIG. 8. Anisotropy of the ESR resonance fields of GaN:Mn^{2+} for sample rotations within the $[1\bar{2}10]$ plane. The experimental resonance positions are indicated with different dot sizes corresponding to their relative intensities. The underlying gray-scale map shows the transition intensities calculated by numerical diagonalization of the spin Hamiltonian. The significantly smaller linewidth of the central $|m_S=1/2\rangle \leftrightarrow |m_S=-1/2\rangle$ fine-structure group makes it possible to distinguish this group from the other resonances even in the strongly overlapping regime around $\theta=60°$.

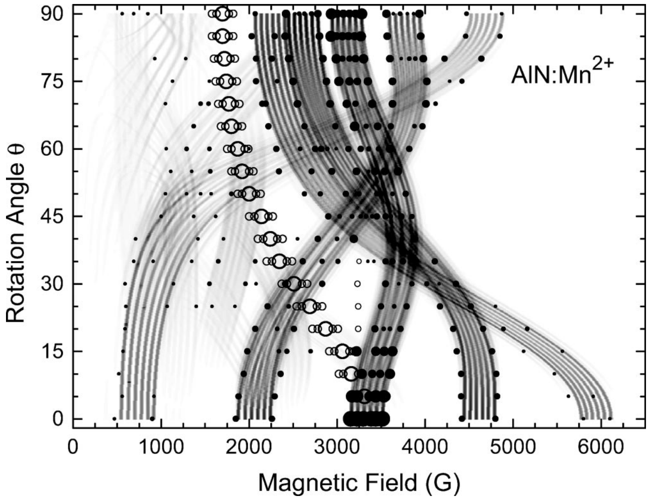

FIG. 9. Anisotropy of the ESR resonance fields of AlN:Mn^{2+}. The hyperfine structure of the outer resonance groups is mostly unresolved because of variations in the fine-structure parameters. However, the lineshapes are sometimes still indicative for a group of overlapping lines. In these cases, the positions of the left and right wings of the resonances are indicated by the dots instead of the central resonance positions. Similar resonances at those positions marked with open circles have been found in the bare sapphire substrate as well, and are therefore not related to the AlN:Mn^{2+} film under investigation.

which are satisfactorily reproduced by the experimental ratios $5:8:11:7:3\pm1$, as can be seen in Fig. 5.

C. Resonance positions and intensities at arbitrary orientations

One of the advantages of ESR spectroscopy in single crystals is the symmetry information, which is accessible by rotation of the sample with respect to the external magnetic field. The resonance positions for $\theta>0°$ allow a critical check of the spin Hamiltonian parameters determined earlier and the verification of the orientation of the axial crystalline field along the *c* axis of the epitaxial layers. The presence of other interactions of Mn spins besides the fine and hyperfine interaction of Mn^{2+} or possible ESR signals from centers which might overlap with the signal from Mn^{2+} at $\theta=0°$, can also be investigated by such experiments.

Approximate solutions for the transitions between the eigenstates of the spin Hamiltonian have been calculated from the perturbation theory in Refs. 26 and 27, including the forbidden transitions with $|\Delta m_I|>0$ discussed below. Those results were supplemented in Ref. 28 with the forbidden half-field transitions with $|\Delta m_S|>1$. Today, the available computing power conveniently enables the exact numerical diagonalization of the spin Hamiltonian matrix. The resonance field positions and transition intensities were obtained with the help of a MATHEMATICA (Ref. 29) code developed by the authors and are shown in Figs. 8 and 9 with the theoretical intensity of the transitions coded by a gray scale. The experimentally observed resonance positions are included in the same plot, with the intensity of the transition coded by the diameters of the dots. The good agreement with the experimental resonance positions measured for Mn^{2+} in GaN and AlN confirms the symmetry of the spin Hamiltonian assumed earlier and the parameters that were determined above from the spectra at $\vec{H}||\mathrm{c}$. Neglecting the contributions from the nuclear spins, the analytical resonance positions $H(\theta)_{m_S\leftrightarrow m_S-1}$ have been calculated to second order in D and to first order in a and F by Refs. 22 and 23:

$$
\begin{aligned}
H(\theta)_{\pm5/2\leftrightarrow\pm3/2} &= [h\nu \mp 2D(3\cos^2\theta-1) \mp 2pa \\
&\quad \mp (1/6)Fq]/(g\mu_B) - 32\Delta_1 + 4\Delta_2, \\
H(\theta)_{\pm3/2\leftrightarrow\pm1/2} &= [h\nu \mp D(3\cos^2\theta-1) \pm (5/2)pa \\
&\quad \pm (5/24)Fq]/(g\mu_B) + 4\Delta_1 - 5\Delta_2, \\
H(\theta)_{+1/2\leftrightarrow-1/2} &= h\nu/(g\mu_B) + 16\Delta_1 - 8\Delta_2, \qquad (7)
\end{aligned}
$$

with the geometry parameters $p=1-5\phi$ and $q=35\cos^4\theta-30\cos^2\theta+3$, and the second-order fine-structure shifts $\Delta_1=D^2/(g\mu_B h\nu)\cos^2\theta\sin^2\theta$, and $\Delta_2=D^2/(4g\mu_B h\nu)\sin^4\theta$. The direction cosines ϕ are defined in Eq. (2) for the $[10\bar{1}0]$ and $[1\bar{2}10]$ rotation planes, respectively. The resulting cubic crystal field splitting between the *A* and *B* lattice sites is visible in the simulations of Figs. 8 and 9; however, no difference between ESR spectra recorded in the two rotation planes was observed experimentally (not shown). From the analytical line positions of Eq. (7), the maximum splitting due to the cubic crystal field occurs at $\theta=60°$ for the $|\pm3/2,m_I\rangle \leftrightarrow |\pm1/2,m_I\rangle$ transition, and is of the order of 6 G for $|a|<10\ \mathrm{G}\times g\mu_B$, which can be assumed in the nitride epitaxial films in analogy to ZnO.[25] Therefore, it is not unexpected to find no experimental difference between the

$[10\bar{1}0]$ and $[1\bar{2}10]$ rotation planes. The splitting between the A and B lattice sites cannot explain the splitting of the central fine-structure group indicated in the simulations of Refs. 5–7.

For intermediate angles, the quantization axis is tilted away from the direction of $\vec{H}$ by the influence of the internal axial crystal field. Therefore, the hyperfine shifts $\Delta h_{m_S,m_I \leftrightarrow m_S-1,m_I}$ of the allowed transitions in Eq. (5) have to be corrected by higher-order terms in A and by mixing cross terms with D, as calculated to second order by Refs. 22 and 27 for the central group $|+1/2,m_I\rangle \leftrightarrow |-1/2,m_I\rangle$:

$$\Delta h(\theta)_{1/2,m_I\leftrightarrow -1/2,m_I} = -\frac{A}{g\mu_B}\left\{ m_I + \frac{A}{2h\nu}(35/4-m_I^2) + \left(\frac{D}{h\nu}\right)^2 [36\sin^2(2\theta)-2\sin^4(\theta)]m_I \right\}. \quad (8)$$

Note, that for $D\approx(1/10)\ h\nu$, as it is the case in these X-band experiments, the magnitude of the third term is almost half of that of the first, so that this correction is indeed required for the analytical field positions.

An even more pronounced effect of the off-diagonal terms $I_xS_x+I_yS_y$ in the spin Hamiltonian is shown in Figs. 8 and 9, where numerical results for the transition intensities in GaN are shown as a function of orientation θ. Due to the mixing of electronic and nuclear quantum numbers, the intensity of the "forbidden" $\Delta m_I \neq 0$ transitions becomes even larger than that of the formerly "allowed" transitions with $\Delta m_I = 0$. According to Refs. 26 and 27, the ratio between the intensity I_f of the first "forbidden" transition $|m_S,m_I\rangle \leftrightarrow |m_S-1,m_I\pm 1\rangle$ and I_a of the "allowed" transition $|m_S,m_I\rangle \leftrightarrow |m_S-1,m_I\rangle$ is given to second-order perturbation theory by

$$I_f/I_a \approx \left[\frac{3}{4}\frac{D}{h\nu}\sin(2\theta)\left(1+\frac{35}{12m_S(m_S-1)}\right)\right]^2 \times(35/4-m_I^2+m_I). \quad (9)$$

Comparison with the exact numerical intensities for GaN in Fig. 10 shows that although qualitatively similar, this analytical result is insufficient to describe the central hyperfine group of Mn^{2+} in GaN correctly at tilt angles of $\theta\approx 10°$, at which the "forbidden" transitions with $\Delta m_I = \pm 1$ (dashed lines in Fig. 10) have grown strongly at the expense of the "allowed" transitions (full lines). At larger tilt angles, only the outmost "allowed" transitions $|+1/2,\pm 5/2\rangle \leftrightarrow |-1/2,\pm 5/2\rangle$ remain visible, and many "forbidden" transitions with $|\Delta m_I|>1$ occur at intermediate angles. Note that the resonance positions for GaN in Fig. 10 have not been assumed fixed as in the simplified calculation of Ref. 27. However, in order to reduce the number of 36 possible traces, the outer and inner transitions for each Δm_I were averaged to a single line. In the case of AlN (not shown), the axial crystal field is tilting the quantization axes even stronger away from the magnetic-field orientation. Therefore, the intensities of the "forbidden" transitions with $\Delta m_I = \pm 1$ increase even more rapidly upon rotation of the sample with respect to the magnetic field and exceed the "allowed transitions" already at $\theta\approx 5°$. The numerical results for the central fine-structure group of both GaN and AlN are shown as gray-scale maps in Figs. 11 and 12. It can be seen from these figures that in contrast to the simulations in Refs. 5–7, the forbidden lines

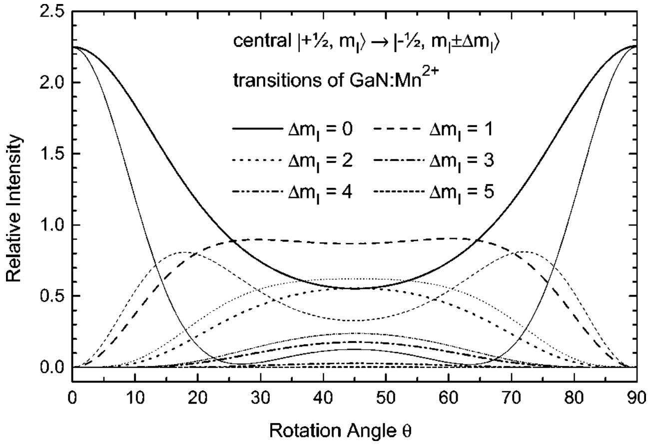

FIG. 10. Angular variation of the $|+1/2,m_I\rangle \leftrightarrow |-1/2,m_I \pm \Delta m_I\rangle$ transition intensities for GaN:Mn^{2+} at a fixed X-band microwave frequency. In order to reduce the number of 36 possible traces, both the two "allowed" and four "forbidden" outer transitions $|\pm 1/2,\pm 5/2\rangle \leftrightarrow |\mp 1/2,\pm 5/2 \mp \Delta m_I\rangle$ were averaged to a single line. Similarly, the intensities of the remaining inner transitions have been averaged and are shown with a second thinner line of the same type for each $|\Delta m_I|$.

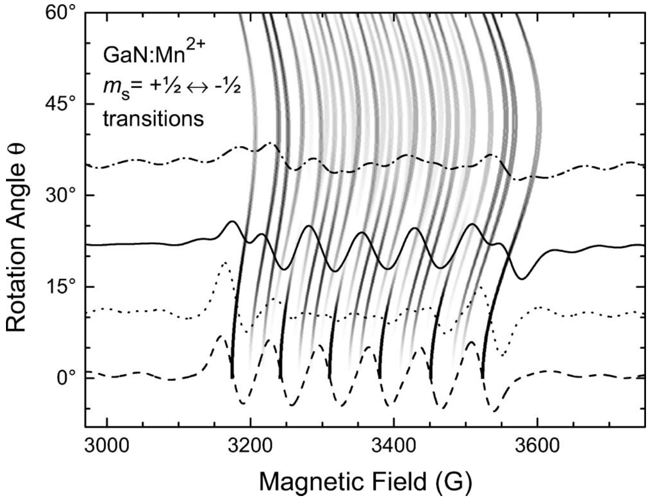

FIG. 11. Magnified view of the inner fine-structure group $|+1/2,m_I\rangle \leftrightarrow |-1/2,m_I \pm \Delta m_I\rangle$ of GaN:Mn^{2+}. The "forbidden" hyperfine satellites are interfering destructively with the "allowed" transitions at tilt angles around $\theta\approx 10°$. The gray-scale map shows the transition intensities of the central fine-structure group obtained from the exact numerical diagonalization without the outer groups, which are broadened experimentally because of the variation of the fine-structure parameters. A large number of resonances at intermediate angles is caused by the appearance of "forbidden" fine-structure transitions, rather than by axial or cubic crystal field splittings of the inequivalent wurtzite lattice sites.

do not split gradually from specific allowed lines at $\theta = 0°$, but rather vanish at magnetic field positions in between those of the allowed transitions.

In GaN, the experimental linewitdh is too large to spectrally resolve both "allowed" and "forbidden" transitions. Rather, the increased number of lines tend to interfere with each other, as can be seen in Fig. 11, where the inner resonances cancel out at $\theta \approx 10°$. It is also evident that at $\theta \approx 20°$ five new resonances appear between the two outmost resonance fields, which correspond to the outer of the six "allowed" transitions at $\theta \approx 0°$. In ZnO:Mn^{2+}, the spectral resolution was limited by similar broad lines,[25] until high-quality crystals made it possible to separate the extremely large number of narrow individual resonance positions.[30] In GaN or AlN, this might be impossible due to strains and ligand hyperfine coupling with the highly abundant nitrogen isotope ^{14}N with $I = 1$, while the natural abundance of the only oxygen isotope ^{17}O with nuclear spin is very low in ZnO.

Due to somewhat smaller linewidths in the central transition group in AlN, some "forbidden" transitions with $\Delta m_I = \pm 1$ are resolved for small misorientations $\theta < 5°$ (Fig. 12). To the second-order perturbation theory,[26] the doublets $|+1/2, m_I\rangle \leftrightarrow |-1/2, m_I - 1\rangle$ and $|+1/2, m_I - 1\rangle \leftrightarrow |-1/2, m_I\rangle$ are split by

$$\begin{aligned} &\Delta h(\theta)_{1/2,m_I \leftrightarrow -1/2,m_I-1} - \Delta h(\theta)_{1/2,m_I-1 \leftrightarrow -1/2,m_I} \\ &\quad = 17A^2/(2g\mu_B h\nu) + 2h\nu(g_I/g)/g\mu_B \\ &\qquad - 25A^3/[g\mu_B(h\nu)^2](m_I - 1/2) \\ &\qquad + 8DA^2/[g\mu_B(h\nu)^2](m_I - 1/2)(3\cos^2\theta - 1) \\ &\qquad - 2P/g\mu_B(m_I - 1/2)(3\cos^2\theta - 1). \end{aligned} \tag{10}$$

Each of the listed terms contributes shifts of several G to the forbidden transition doublet splitting and therefore cannot be neglected in the calculation of these transition fields. The observed spacing of the five pairs of transitions decreases from 30 G on the low-field side to overlapping lines on the high-field side (Fig. 12). This is consistent with the ratio $g_I/g \approx 0.000\,377$ and the reported nuclear quadrupolar moment of ^{55}Mn, which is $P = 0.17$ G$\times g\mu_B$ in ZnO.[25,30]

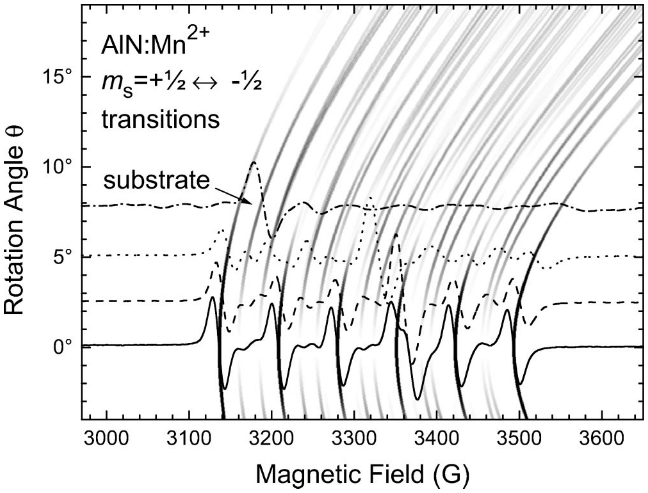

FIG. 12. Magnified view of the inner fine-structure group $|+1/2, m_I\rangle \leftrightarrow |-1/2, m_I \pm \Delta m_I\rangle$ of AlN:Mn^{2+}. The "forbidden" hyperfine satellites interfere destructively with the "allowed" transitions at tilt angles $\theta \approx 5°$. At the best obtained orientation, the "forbidden" lines are small, but still visible. The distinct line moving to lower magnetic fields with increasing tilt angle θ can be attributed to impurities in the sapphire substrate.

In summary, no indication of interactions between adjacent centers was found at a doping level around 10^{20} cm^{-3}. The effective spin Hamiltonian for isolated Mn^{2+} centers sufficiently describes all features of the observed ESR spectra in GaN and AlN at arbitrary orientations. In contrast, exchange narrowing is observed in the ESR spectra of GaAs:Mn^{2+} at doping concentrations around 0.1%, indicating the wave function overlap required for spintronic devices.[31]

IV. DISCUSSION

Manganese is expected to occupy the substitutional cation site in GaN and AlN.[20] Other lattice sites have been reported for Mn in group-III arsenides[32] and will be discussed further below. On the substitutional site, partly ionic and partly covalent bonds to the four nitrogen neighbors bind three electrons of the free Mn [Ar]$3d^5 4s^2$ configuration, resulting in the deep neutral acceptor state Mn^{3+} (A^0), e.g., in GaP,[33] or the antiferromagnetically coupled shallow Mn^{2+}-hole complex in GaAs:Mn.[3] Due to the Jahn-Teller instability of its orbital ground state, large distortions are expected for Mn^{3+} similar to Cr^{2+}.[34,33] Because there is no unperturbed Kramers doublet in the $S = 2$ ground state manifold of these oxidation states, their electron-spin-resonance transitions are possibly shifted outside the range of X-band spectrometers.[34] Additionally, the multiple lines are possibly broadened inhomogeneously by strain effects, so that the spin-resonance signature of Mn^{3+} has been observed in few III–V semiconductors only, most notably GaP.[33] In this work, the neutral Mn^{3+} oxidation state was reduced to the negatively charged acceptor Mn^{2+} (A^-) by the presence of residual donors in GaN:Mn grown at low growth temperatures, or by the Si donors in the GaN:Mn:Si samples.[35]

Theoretical predictions of the parameters g and D of the spin Hamiltonian need to consider spin-orbit coupling in perturbation theory up to very high orders.[36] Without the symmetry-breaking presence of nearby ionic charges, the expected deviations of g from the free-electron value $g_0 = 2.0023$ are small. For substitutional Mn^{2+}, the g factor is typically somewhat reduced from g_0 because of spin-orbit coupling due to the admixture of excited Mn^{2+} states and due to small covalent contributions, in agreement with our observations.[22,36]

Various mechanisms have been suggested to contribute to the observed spin Hamiltonian parameter D. The dominant contributions are crystal fields causing spin-orbit interaction in higher orders, and intermixing from excited Mn^{2+} configurations.[37,38] On the substitutional sites, both contributions are of the order of 10 μeV in magnitude, but of opposite sign. In contrast, the magnitude of D typically exceeds the Zeeman splitting by far for defect complexes.[38,39] In the group-III nitrides, the axial crystal field is probably enhanced by the different bond lengths and the asymmetric charge compensation of Mn^{2+} along the *c* lattice direction.[40] However, theoretical estimates of the zero-field splitting *D* based on higher-order perturbation formulas of the spin-orbit mechanism turned out to be one order of magnitude too small in GaN.[36] As, at the same time, *D* is at least one order of magnitude smaller than expected for a defect complex, it was concluded from the experimental result, from Refs. 5–7 for bulk GaN:Mn crystals, that the Mn^{2+} ion does not occupy the exact Ga^{3+} site, but is displaced by δ towards the N ligand along the *c* lattice direction.[36] Unfortunately, some equations appear inconsistent in the printed version of Ref. 36. Correcting the obvious typographic errors, the axial crystal field parameter due to spin-orbit coupling in the weak-field scheme[38] is given by

$$D_{\mathrm{weak}} \approx \frac{-3\zeta_d^2 B_{20}^2 - 63\zeta_d^3 B_{20}}{70\ P^2 D'} + \frac{-10\zeta_d^2 B_{40}^2 + 7\zeta_d^2 B_{43}^2}{126 P^2 G} \tag{11}$$

with the trigonal crystal field parameters

$$B_{20} \approx \overline{A}_2\left[2\left(\frac{R_0}{R_1}\right)^{t_2} + 3(3\cos^2\Theta - 1)\left(\frac{R_0}{R_2}\right)^{t_2}\right],$$

$$B_{40} \approx \overline{A}_4\left[8\left(\frac{R_0}{R_1}\right)^{t_4} + 3(35\cos^4\Theta - 30\cos^2\Theta + 3)\left(\frac{R_0}{R_2}\right)^{t_4}\right],$$

$$B_{43} \approx -6\sqrt{35}\,\overline{A}_4 \sin^3\Theta \cos\Theta\left(\frac{R_0}{R_2}\right)^{t_4}, \tag{12}$$

the spin-orbit coupling coefficient $\zeta_d \approx 317\ \mathrm{cm}^{-1}$, and $P \approx 25.3\times 10^3\ \mathrm{cm}^{-1}$, $D' \approx 26.9\times 10^3\ \mathrm{cm}^{-1}$, and $G \approx 21.9\times 10^3\ \mathrm{cm}^{-1}$, which can be obtained from the Racah parameters estimated for Mn^{2+} in GaN in Ref. 36 at the reference distance $R_0 = (1/4)R_1(0) + (3/4)R_2(0)$, and with $\overline{A}_2 \approx 10.5\times 10^3\ \mathrm{cm}^{-1}$, $\overline{A}_4 \approx 878\ \mathrm{cm}^{-1}$, and the exponents $t_2 \approx 3$ and $t_4 \approx 5$. The distance $R_1(\delta)$ from the Mn^{2+} ion to the N neighbors along *c* and the distances $R_2(\delta)$ to the three other neighbors oriented at $\Theta(\delta)$ from the Mn site are given by

$$R_1(\delta) = uc - \delta,$$

$$R_2(\delta) = \sqrt{a^2/3 + [c(u - 1/2) - \delta]^2},$$

$$\Theta(\delta) = \arccos\frac{c(u - 1/2) - \delta}{R_2(\delta)}, \tag{13}$$

with the *u* parameter $u_{\mathrm{GaN}} \approx 0.377$,[41] and the lattice constants $c_{\mathrm{GaN}} = (1 + \varepsilon_c)5.1850$ Å, and $a_{\mathrm{GaN}} = (1 + \varepsilon_a)3.1878$ Å.[18] As a_{GaN} and c_{GaN} were measured by x-ray diffraction at room temperature, both lattice parameters must be reduced by approximately 0.06% to account for cooling down to 6 K,[42] at which the ESR parameters were evaluated. With the parameters discussed in Ref. 36, the reported displacement $\delta = 0.07$ Å can be reproduced only, if the variation of $\Theta(\delta)$ is ignored. Using the $\Theta(\delta)$-dependence of Eq. (13), the assumed crystal field parameters of Ref. 36, the *u* parameter of Ref. 41, and the measured lattice constants c_{GaN} and a_{GaN}, the observed spin Hamiltonian parameter *D* is consistent with a displacement of $\delta_{\mathrm{GaN}} = +0.085$ Å. For AlN:Mn^{2+}, a displacement $\delta_{\mathrm{AlN}} = +0.13$ Å would be suggested by the measured lattice constants with $u_{\mathrm{AlN}} \approx 0.382$ (Ref. 41) and the identical set of crystal field parameters, which were estimated based on the optical properties of AlN:Mn^{2+} and on the similarity of the Mn-N bond in GaN:Mn and AlN:Mn. According to Eq. (11), similar results would also result from $\delta_{\mathrm{GaN}} = -0.15$ Å and from $\delta_{\mathrm{AlN}} = -0.24$ Å. These displacements are, however, inconsistent with the observed slope $\partial D_{\mathrm{GaN}}/\partial\varepsilon$, as discussed below. Certainly, the accuracy of the deduced displacements is limited by the various assumptions that are needed for the evaluation of Eq. (11). It is impossible to verify these assumptions and the validity of the crystal field approach with a single experimental crystal field parameter, because the displacements δ are unknown *a priori*, and were chosen to fit this experimental parameter. Also, the good agreement of the weak- and strong-field schemes in Ref. 36 merely supports the validity of the perturbation approximation. It does not verify the assumed parameters and the dominant influence of the spin-orbit coupling over the other contributing mechanisms.

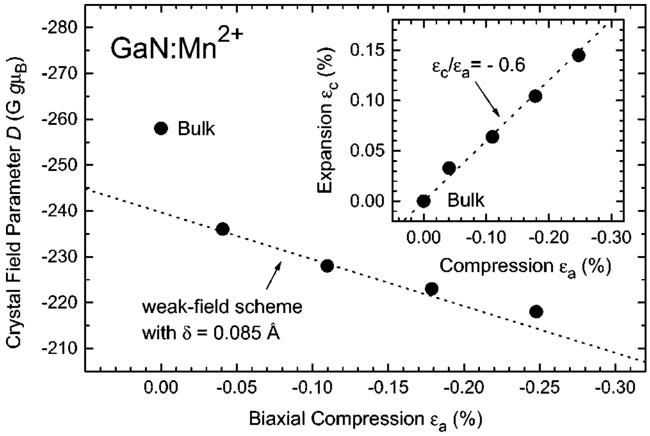

FIG. 13. GaN thin films suffer biaxial strain due to the lattice mismatch to the Al_2O_3 substrate and the cool-down process after growth. The resulting variation of the lattice constants was measured by reciprocal space maps of the asymmetric (2025) reflex of different GaN:Mn and GaN:Mn:Si samples. The linear dependence between the relative changes $\varepsilon_c/\varepsilon_a = -0.6$ corresponds to an effective Poisson ratio $\nu = 0.23$.[18] The bulk GaN crystal of Refs. 5–7 is included with the bulk lattice parameters. The solid line was calculated with Eq. (11) and the parameters of Ref. 36 without any additional free parameters. The good agreement with the experimental data supports the validity of the superposition model for the spin-orbit coupling of Ref. 36.

However, this can be verified independently with the help of ESR measurements on strained GaN films, for which the lattice distortions ε_a and ε_c are known. Similar experiments have been performed and discussed for Mn^{2+} in some other host crystals.[37,38,43] The measured axial crystal field parameters *D* of several GaN:Mn^{2+} and GaNMn^{2+}:Si films are shown in Fig. 13. A variation of the strain is caused in these samples by the heteroepitaxy and the high doping concentrations. The inset shows that the ratio of the strains in these

TABLE I. The chemical trend of the isotropic hyperfine constant A is related to the relative electronegativities of the ligands χ_l and the Mn ions $\chi_{\mathrm{Mn}} \approx 1.5$ eV and to Pauling's covalency parameter $p(\chi_l)$ for the nearest neighbors of the Mn atoms. The axial crystal field is given for the wurtzite materials and for strained GaMnAs, with the conversion factors $1\ \mathrm{G} \times g\mu_B = 0.934 \times 10^{-4}\ \mathrm{cm}^{-1} \times hc = 2.80\ \mathrm{MHz} \times h = 11.6$ neV. The values listed above for bulk GaN are those of Table 1 of Ref. 5. The conversion factor was possibly omitted in the evaluation of the hyperfine splitting $|A_{\mathrm{GaN}}| = 75\ \mathrm{G} \times g\mu_B = 70 \times 10^{-4}\ \mathrm{cm}^{-1} \times hc$ of Refs. 5–7, as a splitting of approximately 70 G was discussed in the text and is shown in the experimental data of Ref. 5.

	χ_l (eV)	$p(\chi_l)$ (%)	A ($\mathrm{G} \times g\mu_B$)	D ($\mathrm{G} \times g\mu_B$)	g	Reference
GaAs (zb.)	2.0	23	-56	(<2)	2.004	31,45
ZnS (zb.)	2.6	20	-68		2.003	22,46
ZnS (wz.)	2.6	20	-70	-113	2.002	46
GaN (wz.) bulk	3.0	17	± 75	± 257	1.999	5–7
relaxed film	3.0	17	-69	-236	1.999	this work
strained film	3.0	17	-69	-218	1.999	this work
AlN (wz.)	3.0	17	-69	-648	2.000	this work
ZnO (wz.)	3.5	14	-79	-253	2.001	25,30,47

films is $\varepsilon_c / \varepsilon_a = -0.6$, as expected.[18] Also shown at the position of the bulk lattice constant of GaN is the axial crystal field parameter measured on the bulk GaN:Mn^{2+} crystal in Refs. 5–7. As the ESR amplitude of the fine-structure satellites of the bulk samples was suppressed by fluctuations of D similar to those shown in Fig. 7, the presence of residual strain must be expected also in these bulk crystals. The reevaluation of the published data of Refs. 5–7 turns out to be consistent with a value of $|D|$ below 250 $\mathrm{G} \times g\mu_B$ as well, which would give a better agreement with the fine-structure parameters determined in this work. The dashed line in Fig. 13 was calculated according to Eq. 11 with $\delta = +0.085$ Å and $\varepsilon_c = -0.6\varepsilon_a$, and corresponds to

$$D \approx (-240 - 1.0 \times 10^4 \varepsilon_a)\mathrm{G} \times g\mu_B, \tag{14}$$

without the assumption of any additional free parameters. For the opposite displacement $\delta_{\mathrm{GaN}} = -0.15$ Å, the slope $\partial D / \partial \varepsilon_a$ would be six times smaller and therefore inconsistent with the experimental data. The almost perfect quantitative agreement convincingly supports the validity of the superposition model of Ref. 36. Nonlinear contributions to $D(\varepsilon_a)$ would be expected from covalent contributions to the spin-orbit coupling,[44] or from strain effects on δ and u, which were assumed as constants here.

An overview of recent results for the isotropic hyperfine splitting A_{GaN} calculated with Green's function method is given in Ref. 19. This splitting is mostly caused indirectly by a Fermi contact interaction of $3d$-induced s orbital spin polarization at the ^{55}Mn nucleus. In the free Mn^{2+} atom, the total core polarization of the inner $1s$, $2s$, and $3s$ orbitals sums up to about $-110\ \mathrm{G} \times g\mu_B$,[32] generating a local magnetic field opposite to the external quantizing field. The induced negative spin density is partly compensated by a positive $4s$ spin density of about $+90\ \mathrm{G} \times g\mu_B$. In a covalent bond, however, this positive contribution is reduced, as the spins are paired off in the binding $4s4p^3$ hybrid orbitals. Therefore, a lower electronegativity of the surrounding ligands leaves a larger negative overall spin density at the Mn nucleus. This subtle balance can be exploited to estimate the valence band spin polarization at the Mn site, which might be of special interest for the determination of the exchange constants required for ferromagnetism in diluted magnetic semiconductors. Additionally, delocalization of the $3d$ electrons and direct $4s$ admixture on the order of 1% can reduce the magnitude of A significantly. These contributions seem to be overestimated in the calculations of Ref. 19, where $|A| = 40\ \mathrm{G} \times g\mu_B$ has been predicted for Mn^{2+} in GaN in contrast to the value of 69 $\mathrm{G} \times g\mu_B$ reported here. The same difference between theory and experiment is found by the authors of Ref. 19 for other transition metal states.

Alternatively to *ab initio* calculations, the expected hyperfine splitting can be estimated with the help of chemical trends between closely related materials. According to Ref. 32, the electronegativities χ_l (see Table I) of the four ligands and of the Mn ion $\chi_{\mathrm{Mn}} \approx 1.5\ eV$ can be used to calculate Pauling's covalency parameter $p(\chi_l)$ of the Mn-ligand bond

$$p(\chi_l) = [1 - 0.16(\chi_l - \chi_{\mathrm{Mn}}) - 0.035(\chi_l - \chi_{\mathrm{Mn}})^2]/4. \tag{15}$$

Selected semiconductor materials with anion electronegativities χ_l close to that of nitrogen are listed in Table I, together with the covalency $p(\chi_l)$ of the Mn-anion bond and the hyperfine constants for substitutional Mn^{2+} on the cation site. Obviously, the hyperfine constants for GaN:Mn^{2+} and AlN:Mn^{2+} fit in between the numbers for ZnS and ZnO, as would be expected from the electronegativity on N, which is between those of S and O; twice as large hyperfine constants have been reported for Mn^{2+} on tetrahedral interstitial lattice sites in GaP and GaAs,[32] which confirms the substitutional nature that was assumed above. With respect to the covalency and hyperfine constants, similarities to Mn in II–VI semiconductors rather than to III–V materials such as GaAs are expected, as long as the neutral Mn^{3+} centers can be reduced to Mn^{2+} by residual donors or Si codoping, as in the samples discussed here.

V. SUMMARY

The ESR signature of Mn^{2+} was observed and analyzed in Mn-doped MBE-grown GaN and AlN films. All observed transitions are consistent with the spin Hamiltonian for isolated substitutional $^{55}\mathrm{Mn}^{2+}$ centers with $g_{\mathrm{GaN}}=1.9994$, $g_{\mathrm{AlN}}=2.0004$, $D_{\mathrm{GaN}}=-218$ to $-236\ \mathrm{G}\times g\mu_B$, and $D_{\mathrm{AlN}}=-648\ \mathrm{G}\times g\mu_B$, $(a-F)_{\mathrm{GaN}}=+6\ \mathrm{G}\times g\mu_B$, $(a-F)_{\mathrm{AlN}}=+10\ \mathrm{G}\times g\mu_B$, and $A=-69\ \mathrm{G}\times g\mu_B$ both for GaN and AlN. The differences of the axial crystal field parameters are correlated with the macroscopic strain in our GaN:Mn films and agree well with predictions of the superposition theory of crystal fields. Intermixing of the spin eigenstates at intermediate orientations strongly enhances the transition probabilities of the usually "forbidden" transitions with $\Delta m_I>0$, which is confirmed by the experimental and numerical results. It is concluded that the paramagnetic Mn^{2+} impurities occupy almost substitutional sites in GaN and AlN. At the investigated Mn concentration of $10^{20}\ \mathrm{cm}^{-3}$, they are present as isolated paramagnetic centers, and exchange effects are negligible.

ACKNOWLEDGMENTS

The authors acknowledge financial support from Deutsche Forschungsgemeinschaft (SFB 348). They are thankful to L. Görgens for the determination of the Mn concentrations by ERD.

---

*Electronic address: tobias.graf@wsi.tum.de

[1] M. Oestreich, Nature (London) **402**, 735 (1999).
[2] T. Dietl, H. Ohno, and F. Matsukura, Phys. Rev. B **63**, 195205 (2001).
[3] J. Schneider, U. Kaufmann, W. Wilkening, M. Baeumler, and F. Köhl, Phys. Rev. Lett. **59**, 240 (1987).
[4] T. Dietl, F. Matsukura, and H. Ohno, Phys. Rev. B **66**, 033203 (2002).
[5] P.G. Baranov, I.V. Ilyin, and E.N. Mokhov, Mater. Sci. Forum **258-263**, 1167 (1997).
[6] P.G. Baranov, I.V. Ilyin, and E.N. Mokhov, Solid State Commun. **101**, 611 (1997).
[7] P.G. Baranov, I.V. Ilyin, E.N. Mokhov, and A.D. Roenkov, Semicond. Sci. Technol. **11**, 1843 (1996).
[8] P.G. Baranov *et al.*, MRS Internet J. Nitride Semicond. Res. **3**, 50 (1998).
[9] M. Zając, R. Doradziński, J. Gosk, J. Szczytko, M. Lefeld-Sosnowska, M. Kamińska, and A. Twardowski, Appl. Phys. Lett. **78**, 1276 (2001).
[10] R.Y. Korotkov, J.M. Gregie, and B.W. Wessels, Appl. Phys. Lett. **80**, 1731 (2002).
[11] M.L. Reed, N.A. El-Masry, H.H. Stadelmaier, M.K. Ritums, M.J. Reed, C.A. Parker, J.C. Roberts, and S.M. Bedair, Appl. Phys. Lett. **79**, 3473 (2001).
[12] T. Sasaki, S. Sonoda, Y. Yamamoto, K. Suga, S. Shimizu, K. Kindo, and H. Hori, Appl. Phys. Lett. **91**, 7911 (2002).
[13] G.T. Thaler *et al.*, Appl. Phys. Lett. **80**, 3964 (2003).
[14] G.E. Archangelskii, F. Karel, J. Mareš, S. Pačesová, and J. Pastraňák, Phys. Status Solidi A **69**, 173 (1982).
[15] O. Ambacher, J. Phys. D **31**, 2653 (1998).
[16] G. Dollinger, C.M. Frey, A. Bergmaier, and T. Faestermann, Europhys. Lett. **42**, 25 (1998).
[17] H. Yang, H. Al-Brithen, A.R. Smith, J.A. Borchers, R.L. Cappelletti, and M.D. Vaudin, Appl. Phys. Lett. **78**, 3860 (2001).
[18] C. Kisielowski *et al.*, Phys. Rev. B **54**, 17 745 (1996).
[19] U. Gerstmann, A.T. Blumenau, and H. Overhof, Phys. Rev. B **63**, 075204 (2001).
[20] A. Zunger, Solid State Phys. **39**, 275 (1986).
[21] C.A. Bates and K.W.H. Stevens, Rep. Prog. Phys. **49**, 786 (1986).
[22] A. Abragam and B. Bleaney, *Electron Paramagnetic Resonance of Transitions Ions* (Oxford University Press, Oxford, 1970).
[23] J.W. Orton, *Electron Paramagnetic Resonance* (Iliffe Books, London, 1968).
[24] J. Schneider, Z. Naturforsch. A **17A**, 189 (1962).
[25] J. Schneider and S.R. Sircar, Z. Naturforsch. A **17A**, 570 (1962).
[26] J. Schneider and S.R. Sircar, Z. Naturforsch. A **17A**, 651 (1962).
[27] B. Bleaney and R.S. Rubins, Proc. Phys. Soc. **77**, 103 (1961); corrigendum Proc. Phys. Soc. **78**, 118 (1963).
[28] B. Clerjaud, C. Marti, and A. Billmann, Phys. Status Solidi B **44**, 693 (1971).
[29] S. Wolfram, *Mathematica* (Addison-Wesley, Redwood City, 1991).
[30] A. Hausmann and H. Huppertz, J. Phys. Chem. Solids **29**, 1369 (1968).
[31] O.M. Fedorych, E.M. Hankiewicz, and Z. Wilamowski, Phys. Rev. B **66**, 045201 (2002).
[32] S.J.C.H.M. van Gisbergen, M. Godlewski, T. Gregorkiewicz, and C.A.J. Ammerlaan, Phys. Rev. B **44**, 3012 (1991).
[33] J. Kreissl, W. Ulrici, M. El-Metoui, A.M. Vasson, A. Vasson, and A. Gavaix, Phys. Rev. B **54**, 10 508 (1996).
[34] J.T. Vallin and G.D. Watkins, Phys. Rev. B **9**, 2051 (1974).
[35] T. Graf, M. Gjukic, M. Brandt, M. Stutzmann, and O. Ambacher, Appl. Phys. Lett. **81**, 5159 (2002).
[36] W.C. Zheng, S.Y. Wu, and J. Zi, Z. Naturforsch., A: Phys. Sci. **56**, 473 (2001).
[37] W.L. Yu and M.G. Zhao, Phys. Rev. B **37**, 9254 (1988).
[38] D.J. Newman and B. Ng, Rep. Prog. Phys. **52**, 699 (1989).
[39] J. Kreissl, W. Gehlhoff, P. Omling, and P. Emanuelsson, Phys. Rev. B **42**, 1731 (1990).
[40] W. Low and J.T. Suss, Phys. Rev. **119**, 132 (1960).
[41] O. Ambacher *et al.*, J. Phys.: Condens. Matter **14**, 3399 (2002).
[42] K. Wang and R.R. Reeber, Mater. Res. Soc. Symp. Proc. **482**, 863 (1998).
[43] C. Blanchard, R. Parrot, and D. Boulanger, Phys. Rev. B **7**, 4072 (1973).
[44] G.E. Barberis and G.B.M.R. Calvo, Phys. Rev. B **49**, 8583 (1994).
[45] N. Almeleh and B. Goldstein, Phys. Rev. **128**, 1568 (1962).
[46] S.P. Keller, I.L. Gelles, and W. Smith, Phys. Rev. **110**, 850 (1958).
[47] P.B. Dorain, Phys. Rev. **112**, 1058 (1958).